METAL OXIDE NANOPARTICLES FORMED FROM SOLUTION DROPLETS UNDER HIGH HEATING RATE

F. Carbone*, A. Barone**, F. Beretta* and A. D'Anna***

francesco.carbone@irc.cnr.it

* Istituto di Ricerche sulla Combustione, Consiglio Nazionale delle Ricerche,
piazzale Vincenzo Tecchio 80, 80125 Napoli, Italy
** Istituto Italiano di Tecnologia, via Morego 30, 16163 Genova, Italy
*** Dipartimento di Ingegneria Chimica, Università degli Studi di Napoli Federico II,
piazzale Vincenzo Tecchio 80, 80125 Napoli, Italy

Abstract

The formation mechanisms of combustion generated metal oxide nanoparticles were explored in a stoichiometric laminar premixed flame doped with droplets of cadmium, nickel(II) and lead(II) nitrate aqueous solutions. Generated particles were thermophoretically collected and analyzed by Atomic Force Microscopy (AFM). The results showed that most of the particles have sizes lower than 10nm. The size distribution function shapes and time evolutions depend on the metal salt solubility and thermal decomposition characteristics. By comparing the thermophoretically collected matter and the amount of injected metal precursors, a size dependent adhesion efficiency of the particles on probe mica plates has been found. The results showed that nanoparticles have a low capability to adhere on a surface, regardless of the used metal. The adhesion efficiency quickly decreases for particles smaller than 10nm. As a consequence, the smallest particles are present in the flame with a relative high number concentration. This feature is of great interest when developing filtering systems able to remove nanoparticles with size lower than 10nm at the exhaust of combustion systems.

Introduction

Combustion systems are the main sources of particulate matter in urban areas. Particles are released in the atmosphere in a wide size range implying a severe pollution problem since particulate matter may contribute to climate change and have strong adverse health effects [1]. Recent toxicological studies have shown that particle toxicity depends on particle number density and increases as particle size decreases [2]-[4]. Moreover, the efficiency of filtering devices also decreases with particles size [5]. Therefore, the formation of combustion generated nanoparticles, particularly those in the ultrafine range, requires further investigations.

While carbonaceous particles produced in fuel rich conditions have been widely studied in the entire size range they are released [6]-[8], less efforts have been spent to investigate metal particles with size below 10nm. Metals, always contained into wastes, crude oils, coals and biomass, are introduced into combustion system in many forms but, after some physical and chemical transformations, they are released as bottom or volatile ashes in the same amount they are introduced [1][9]. Recently we have found that particles smaller than 10 nm are generated in a large amount during pulverized coal combustion being both carbonaceous and metals [10]-[12]. Metal nanoparticles are generated by burning every ash-containing fuel. Therefore the investigation of particle formation, coagulation and collection at high temperatures is crucial in understanding their emission from real combustion devices [13]-[14].

The fate of toxic metals in combustion-like environments has been already studied by heating-up droplets of metal nitrate aqueous solutions into a drop-tube furnace [15]-[16] and

injecting metal salt powders in a flame [17]. Nanoparticles smaller than 10nm were not detected, probably because of the presence of larger particles obscuring the presence of the smaller one and because of the used diagnostic techniques. Attempts to study metal oxide nanoparticle formation in flame and tubular reactor were performed by many authors [18]. Recently, Fennell et al. [19] have shown the formation of particles smaller than 10nm by feeding metal chloride water solution droplets in a flame.

In this paper we report a laboratory study performed to investigate metal nanoparticles generated in combustion environments. We measure the size distributions, in a size range extending down to few nanometers, of particles produced from droplets of metal nitrate solutions in air quickly heated by exhaust gas of a premixed flame of ethylene/air. The flame burnt gas provides the heat transfer for the fast heating and transformation of the droplets containing the metal particle precursors.

The generated nanoparticles are thermophoretically sampled at several heights above the burner (HAB) to follow their time evolution. Dimensional analysis is performed by Atomic Force Microscopy (AFM) [20]-[22] whereas Scanning Electron Microscopy (SEM) with Energy Dispersive X-ray Spectroscopy (EDXS) of collected particles was performed to get information on their elemental composition.

A nanoparticle formation pathway is proposed and the influence of precursor metal properties on the process is discussed. Particular emphasis is focused on particle adhesion efficiencies because of its importance on the emission of such small particles at the exhausts of furnaces.

Experimental

Flame reactor and operating conditions

A water-cooled porous-plug brass burner (McKenna Products) is used to stabilize a flat laminar premixed flame of stoichiometric ethylene and air (cold gas flow velocity of 80 mm/s). The burner is drilled on its axis where a 7.5mm ID stainless-steel tube is inserted. Monodisperse droplets (size of about 40 μm) of metal particle precursors are dispersed into 600cm^3/min of air to prevent coalescence. Both droplets and air are fed through the tube coaxially to the flame reactants. The heat transfer from the flame hot burnt gas to the aerosol results in the fast heating and evaporation of the droplets. The droplets are generated by a Berglund-Liu-type Vibrating Orifice Aerosol Generator (model 3450, TSI) using a 20μm orifice oscillating at a frequency of 60KHz. The particle precursor solution flow is 139μl/min but about 30% is lost in the adduction tube, not reaching the flame. This amount is properly drained and quantified during each measurement.

Table I. Selected physical properties of metal nitrates and expected products.

	Chemical Formula	MW g/mol	Melting point (K)	Boiling point (K)	Solubility wt% (25°C-100°C)	Density (g/cm^3)	Color
Precursor	Cd(NO$_3$)$_2$	236.4	633		61.0-87.4	3.6	white
	Ni(NO$_3$)$_2$	182.7			49.8-69.0		green
	Pb(NO$_3$)$_2$	331.2	743		37.4-56.8	4.5	colorless
Expected Products	CdO	128.4		1832sub	insoluble	8.1	brown
	NiO	74.7	2230		insoluble	6.7	light green
	PbO (Massicot)	223.2	1163	1750	insoluble	9.6	yellow

data form: David R. Lide, ed. (2007). *CRC Handbook of Chemistry and Physics.* Boca Raton, FL, Taylor and Francis.

Three aqueous solutions of metal salts have been analyzed. They contain 25% mass concentration of cadmium nitrate Cd(NO$_3$)$_2$, nickel(II) nitrate Ni(NO$_3$)$_2$ and lead(II) nitrate Pb(NO$_3$)$_2$. The solutions are prepared dissolving in bidistilled water cadmium nitrate

tetrahydrate $Cd(NO_3)_2$-$4H_2O$, nickel(II) nitrate hexahydrate $Ni(NO_3)_2$-$6H_2O$ and $Pb(NO_3)_2$ salts, respectively. These salts have been chosen because they cover a wide range of solubility in water. Moreover the three metals have largely different volatility and they are abundant in fossil fuels and wastes [9]. Table I reports the physical properties of metal nitrate and that of the expected products after the heating.

Metal solution droplets dispersed in air are fed coaxially to the hot burnt gas of a stoichiometric, particle-free, blue flame. The addition of the solution droplets into the exhaust flame gases causes the appearance of a light emitting jet in the center of the reactor. The jet flickering is reduced placing a 3mm thick flat stabilization plate at HAB=40mm. The plate is made of brass and it has a central 10mm hole.

Flame temperature is measured along the reactor axis by a 125μm Pt/Pt-13%Rh thermocouple (Type R, Omega Engineering). During temperature measurements, bidistilled water without metal precursors is feed through the tube. This procedure prevents metal particle deposition on the thermocouple junction. Particle residence times in the reactor are evaluated assuming particle velocity equal to that of hot gases.

Thermophoretic sampling for microscopy analysis
Particles formed along the flame reactor are thermophoretically collected on mica muscovite disks (3mm diameter and 0.2mm thick) inserted parallel to the gas streamline using a pneumatic actuator that assures a quick insertion of the disk. Different sampling times have been tested in order to find the minimum sampling time (about $\Delta t \sim 30ms$) to collect reasonable amount of material for subsequent analysis. Usually, with a sampling time of 30ms, a particle number density from 200 to 500 particles/μm^2 is collected.

The samples are analyzed by atomic force microscopy operating in tapping-mode (Nanoscope IIIa™, Digital Instruments). A topological three-dimensional image of the deposited particles is generated with a resolution of about 1-2 nm for x/y axes and of about 0.1nm for the z axis. This resolution allows resolving particles with volume as small as $1nm^3$ regardless of their shape. An advanced image processing software (S.P.I.P.™, ImageMetrology) is used to measure the particle volumes, baseline areas, and maximum heights above the substrate. Particle equivalent diameter (*D*) and Aspect Ratio (*AR*) are calculated as the diameter of a sphere having the measured volume and the height to baseline width ratio, respectively. AR gives information on particles morphology.

AFM analysis allows evaluating the volume fraction of the particles. Indeed, volume fraction is the ratio between the total volume of collected particles (Vol_{part}) and the sampled gas volume (Vol_{samp}). The volume of the sampled gas is calculated considering the thermophoretic flow due to the presence of a laminar boundary layer above the mica surface, assumed at constant temperature (T_{mica}=300K). It is the product of the imaged area (A_{im}) by the particle thermophoretic velocity (V_{th}) and the sampling time:

$$fv_{AFM} = \frac{Vol_{part}}{Vol_{samp}} = \frac{Vol_{part}}{A_{im} \cdot V_{th} \cdot \Delta t}$$

(1)

The thermophoretic velocity depends on the thermal gradient (∇T) regardless of the particle sizes, since the particles are within the free molecular regime [23]-[24]:

$$V_{th} = 0.55 \cdot \nu \cdot \frac{\nabla T}{T} \approx 0.55 \cdot \frac{\nu}{T_{film}} \cdot \frac{T_{gas} - T_{mica}}{\delta_{th}}$$

(2)

It can be calculated by the ratio of the temperature difference by the thickness (δ_{th}) of the thermal boundary layer on a flat surface. Gas kinematic viscosity (ν)is evaluated at the actual absolute temperature assumed to be equal to the film temperature (T_{film}). The film temperature is calculated as the average of gas and mica temperatures.

The collected AFM data are quite repeatable. The problem of the spatial non-uniformity of the thermal boundary layer thickness is overcome by the small size (usually 2x2 μm^2) and the high position accuracy of the imaged area. The substrate only slightly heats up during sampling and a temperature increase of 100K does not significantly modify the thermophoretic velocity and thus the calculated volume fraction.

A selected number of samples are also collected on aluminum substrates (20mm diameter) for scanning Electron Microscopy (SEM) and Energy Dispersive X-ray Spectroscopy (EDXS) analysis. Measurements are performed on the flame axis inserting the substrate perpendicularly to the gas streamline. One hundred substrate insertions in flame are required to collect enough matter for the analysis. The samples are examined by a Philips XL30 SEM with a LaB6 filament equipped with an EDXS DX-4i microanalysis device to determine particle elemental composition.

Results and Discussion

Metal particle precursors are injected in the flame exhaust gas in the form of monodisperse droplets (40 μm diameter) of aqueous solutions which contain 25% mass concentration of cadmium nitrate, nickel(II) nitrate and lead(II) nitrate, respectively.

The axial reactor temperature profile results from the heat transfer from the ethylene flame hot products to the cold air transporting the particle precursor droplets. Temperature increases almost linearly from ambient to approximately 1200K for heights above burner up to 20mm and it remains almost constant around this value for larger heights above burner. A scheme and a picture of the reactor and the temperature profile are reported elsewhere [21]. Droplets are injected at the burner mouth and quickly vaporize delivering the particle precursors in the gas phase. The droplet evaporation completes at 20mm as verified both by AFM and SEM analyses, corresponding to a residence time in the flame of about 20ms. In this time interval, particle precursor reactions occur mainly in the aqueous solutions. The precursor compounds heating rate is of the order of 10^4K/s. Thereafter, metal compounds evolve in the high-temperature gas phase in which they are released.

The pure ethylene/air flame is blue colored and particle free as determined by laser light scattering measurements. A red colored jet appears by adding the $Cd(NO_3)_2$ solution droplets whereas the jet color ranges from yellow to red supplying both $Ni(NO_3)_2$ and $Pb(NO_3)_2$ solutions. Also the deposits collected on the stabilizer plate placed at 40mm above the burner change their characteristics by changing the fed solutions: orange-brown powder is deposited by $Cd(NO_3)_2$, white-grey deposit is collected using $Ni(NO_3)_2$ and white-yellow-brown residue is generated from $Pb(NO_3)_2$.

Table II. Calculated volume fractions of generated particles

Precursors	Expected Products	*Fv, ppm*
$Cd(NO_3)_2$	CdO	1.2
$Ni(NO_3)_2$	NiO	1.0
$Pb(NO_3)_2$	PbO (Massicot)	1.0

Particle volume fraction (*fv*) in the flame is estimated by a material balance of the fed metal. The particle density is supposed equal to that of bulk metal oxides expected as products. The calculated values are reported in Table II. The estimated volume fraction of particles generated from the $Pb(NO_3)_2$ solution agrees very well with that measured by in-situ

UV-visible light extinction [21]-[22] supporting the possibility to estimate metal particle volume fraction simply by a material balance and showing that the most of the metal compounds are in a condensed phase at the points where measurements have been performed.

Nanoparticles generated by the precursor transformation are thermophoretically sampled on the reactor axis from HAB=20mm to 35mm, stepwise of 5mm corresponding to a residence time in flame, elapsed between successive sampling points, of about ~4ms. Dimensional analysis is performed by AFM on the sampled material whereas SEM with EDXS is performed to get information on the chemical composition of the sampled particles.
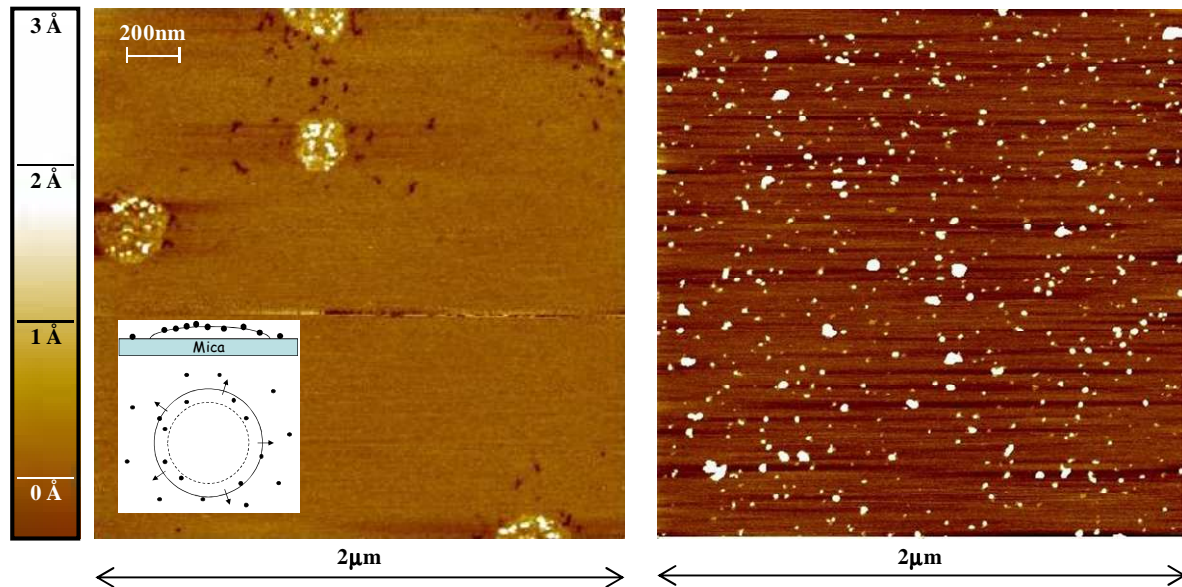

Figure1. Typical AFM images of the particles sampled along the reactor axis slightly upstream of HAB=20mm (left side) and at higher sampling locations (right side). The insert on the left side reports a schematization of the nanoparticle formation inside the droplets.

AFM images of the material collected close to the burner mouth, namely slightly upstream of 20mm above the burner, show some incompletely evaporated droplets deposited on the substrate resulting in large flat entities. Nanoparticles (nanometric protrusions) emerge from such entities, as evidenced in the AFM image reported on the left side of Fig.1. SEM images of the samples collected at these heights also show large objects whose EDX analysis reveal to be composed of the injected metal, nitrogen and oxygen. These objects shrink under the effect of the electron beam. It appears that metal nitrates nucleate close to the droplet surface as the solution approaches saturation because of water vaporization, as suggested by Limaye and Helble [25]. Nuclei can slightly grow and coagulate in the liquid medium before being released in the gas-phase because of fast water vaporization. Conversely, AFM images obtained at higher sampling locations (starting from 20mm) show the presence of isolated particles (left side of Fig.1). At these heights SEM images do not show isolated particles due to the longer total sampling time, but they show a layer of particles whose size are below the instrument resolution.

The statistics on the results of AFM dimensional analyses are performed only on the images of samples containing isolated particles. Collected particle number is converted in the normalized frequency distributions of the diameters. The latter are fitted by the sum of two log-normal distributions allowing data easily handling:

$$\frac{1}{N}\frac{dN}{dD_p} = \frac{w}{D_p \log(\sigma_1)\sqrt{2\pi}}\exp\left\{-\frac{1}{2}\left[\log\left(\frac{D_p}{MD_1}\right)\middle/\log(\sigma_1)\right]^2\right\}+$$

$$+\frac{(1-w)}{D_p \log(\sigma_2)\sqrt{2\pi}}\exp\left\{-\frac{1}{2}\left[\log\left(\frac{D_p}{MD_2}\right)\middle/\log(\sigma_2)\right]^2\right\}$$

(4)

The number fraction of particles in the first mode (w) and the median diameters (MD_1 and MD_2) and the widths (σ_1 and σ_2) of the two modes are the parameters used to reproduce the experimental data. N is the total number of the analyzed particles.
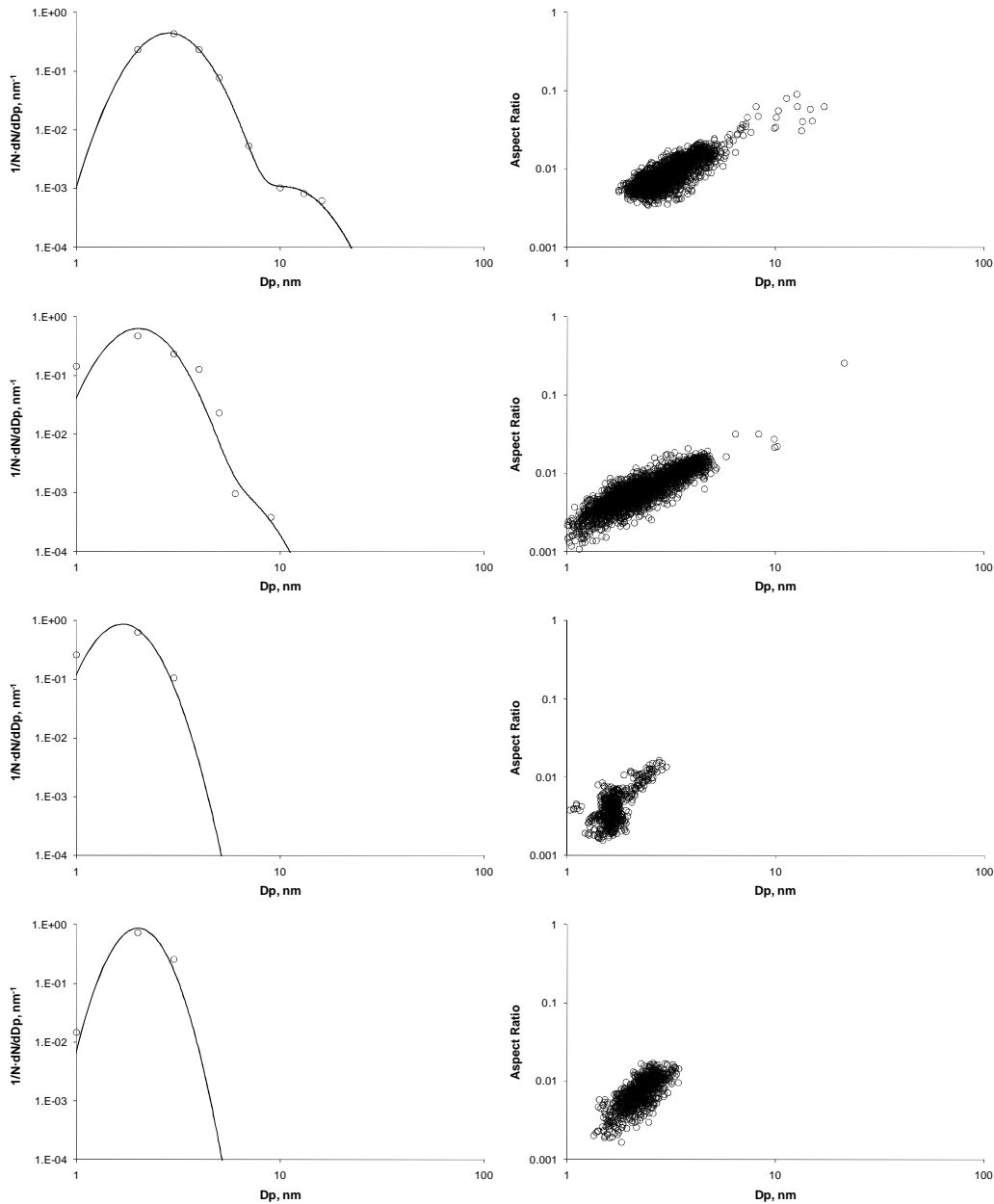

Figure 2. (left side) particle size distribution functions and (right side) aspect ratios measured along the flame axis when injecting cadmium nitrate. From the bottom to the top: 20, 25, 30 and 35mm.

Figure 2 (left side) shows the size distributions of particles collected at different heights above the burner when cadmium nitrate containing droplets are injected in the flame. Points are obtained by AFM analysis and the dotted lines are their best fit with the parameters reported in Table III. At HAB=20mm, particles are almost monodisperse with 2.2nm mean diameter ($<D>$). Almost the same size distribution (2.0nm $<D>$) is obtained at HAB=25mm. The appearance of a second mode in the size distribution having a $<D>$ of 6.3nm, is observed at HAB=30mm. The particles into the second mode represent just 0.5% of total number while the first mode still have $<D>$ of 2.3nm. At HAB=35mm the first mode slightly grows (3.2nm $<D>$). The relative number of particles into the second mode (1%) is doubled with respect to the previous height and also the mean diameter (12.7nm) increases.

Table III. Parameters to fit the size distribution functions obtained by the AFM image analyses.

Precursor	HAB[mm]	w	MD$_1$[nm]	MD$_2$[nm]	σ$_1$	σ$_2$
Cd(NO$_3$)$_2$	20	1	2.1	-	1.25	-
	25	1	1.8	-	1.30	-
	30	0.995	2.2	6	1.35	1.40
	35	0.99	3.1	12	1.35	1.40
Ni(NO$_3$)$_2$	20	0.97	3.3	12	1.30	1.40
	25	0.95	3.1	10	1.30	1.50
	30	0.85	3.2	5.4	1.30	1.30
	35	1	4.1	-	1.25	-
Pb(NO$_3$)$_2$	20	0.75	5.8	14	1.50	1.60
	25	0.75	5.8	14	1.50	1.50
	30	0.80	4.1	14	1.40	1.50
	35	0.80	2.8	12	1.30	1.40

Figure 2 (right side) also shows the aspect ratio of the collected particles as a function of their diameter. Particles belonging to the first mode of size distributions have *AR* lower than 0.03. The second mode particle *AR* range from 0.03 to 0.2. The observed low values indicate a liquid-like behavior of the nanoparticles. Their base shows an almost circular shape suggesting they could be spherical into the flame but they deform impinging on the substrate [20]-[21],[26]-[27].

Figure 3 summarizes the results reported in Fig.2a showing the change along the flame axis of the mean diameters of the first and second mode particles.
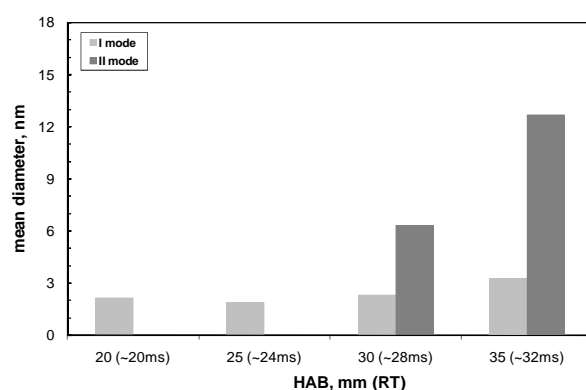

Figure 3. Mean diameters of the particles belonging to the first (I mode) and second mode (II mode) of the particle size distribution along the flame axis when injecting cadmium nitrate.

SEM analyses of the particles collected on the aluminum substrates show that the stub is covered by a layer of ultrafine particles with sizes well below the instrumental resolution. The

EDXS analyses reveal the presence of cadmium and oxygen. A small amount of nitrogen is detected at HAB=20mm whereas nitrogen is completely absent at the other sampling locations, indicating that cadmium oxide particles have been synthesized. Unfortunately the detector is not sufficiently sensitive in detecting oxygen to determine the exact oxidation degree of the powder.

Cadmium nitrate has the highest solubility in water among the three chosen metal salts and it nucleates inside the water droplets toward the end of the evaporation process. $Cd(NO_3)_2$ nuclei have not enough time to aggregate, grow or diffuse inside the droplet since the evaporation process is almost completed and they are released in the high-temperature gas-phase. $Cd(NO_3)_2$-$4H_2O$ droplets dehydrates at 484K, thereafter the $Cd(NO_3)_2$ nuclei decomposes to CdO at 674K [28] in the gaseous environment causing the shrinking of the nuclei and the generation of particles detected at 20 and 25mm. CdO evaporation can also occur but its further thermal decomposition is not allowed at ~1200K. Along the flame axis CdO particles slightly grow due to coagulation and a particle second mode appear at 30mm. CdO is liquid at the flame temperature and nanoparticles show a plastic morphology upon impact on the substrate as shown by the very low values of the aspect ratio of the collected particles also in the whole size range. This behavior is more pronounced for smallest particles that have the smallest ARs.

A different behavior is exhibited by $Ni(NO_3)_2$ and $Pb(NO_3)_2$ which have a lower solubility in water and different dehydration and decomposition temperatures.

Figure 4 (left side) shows the particle size distribution functions obtained by AFM analysis and their best fitting (parameters in Table III) when $Ni(NO_3)_2$ is injected into the flame. A bimodality in the particle size distribution function is observed from the beginning of the transformation process whereas particles are almost monodisperse at longer residence times.

At HAB=20mm the size distribution function of collected particles is characterized by 3.4nm $<D>$ for the first mode and by 12.7nm $<D>$ for the second mode, the latter representing 3% of particles number. At HAB=25mm first mode $<D>$ (3.2nm) is slightly smaller while the second mode (5% of particles number) shrinks significantly (10.8nm MD). At HAB=30mm the first mode still have 3.3nm $<D>$ while the second mode, subjected to a further shrink (5.6nm $<D>$), is collapsing into the first mode. The second mode completely disappears at HAB=35mm where almost monodisperse particles (4.2nm MD) are sampled.

The initial bimodal nature of the size distribution probably depends on the $Ni(NO_3)_2$ solubility in water and the temperatures at which $Ni(NO_3)_2$-$6H_2O$ thermal decompositions occur [29]. Nickel(II) nitrate dehydrates between 418K-463K so that $Ni(NO_3)_2$ nucleates already in the $Ni(NO_3)_2$-$6H_2O$ droplets. Therefore, nuclei are able to slightly grow and some of them aggregate forming larger particles before emerging from the droplets.

The smallest formed particles are already larger than those generated from $Cd(NO_3)_2$ solution because of the lower solubility and dehydration temperature speeding up the nucleation in the droplet. The nuclei are quickly heated in the gaseous environment and decomposed into NiO (573K). The shrinking of the second mode observed downstream in the flame could be due to the decomposition of the larger nitrate particles. Indeed, the size reduction is compatible with the particles loss of mass involved in the $Ni(NO_3)_2$ to NiO decomposition. The NiO evaporation or further thermal decomposition is not allowed at ~1200K.

The EDXS analyses on the SEM substrates confirm the presence of nickel, oxygen and nitrogen, the latter being more abundant at the first height and completely absent only at HAB=35mm where second mode particles are not present.
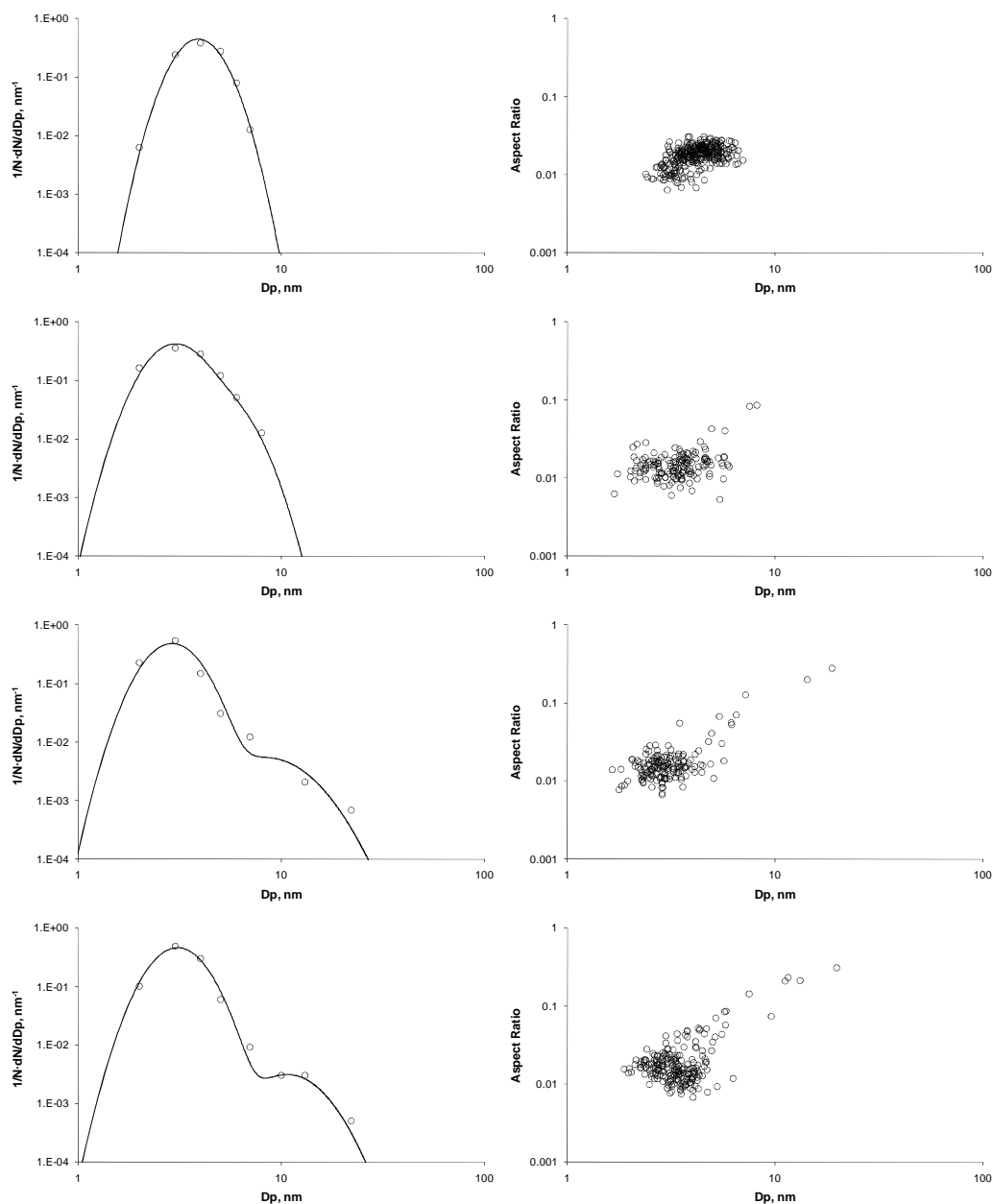
Figure 4. (left side) particle size distribution functions and (right side) aspect ratios measured along the flame axis when injecting nickel(II) nitrate. From the bottom to the top: 20, 25, 30 and 35mm.

Figure 4 (right side) also shows *AR* plotted versus particle diameter. Particles in the first mode have AR lower than 0.05 similar to the $Cd(NO_3)_2$ formed particles, indicating a liquid-like nature for such particles. The second mode particles have AR as high as 0.3, larger than the AR for the same size $Cd(NO_3)_2$ formed particles, indicating a less plastic nature for the larger particles.

The process of particle formation is summarized in Fig.5 where the change along the flame axis of the mean diameters of the first and second mode particles is reported. Large size $Ni(NO_3)_2$ particles nucleate in the liquid phase; once released in the high temperature gas-phase they decompose into smaller NiO particles. At the end of the process only small NiO particles remain in the reactor.
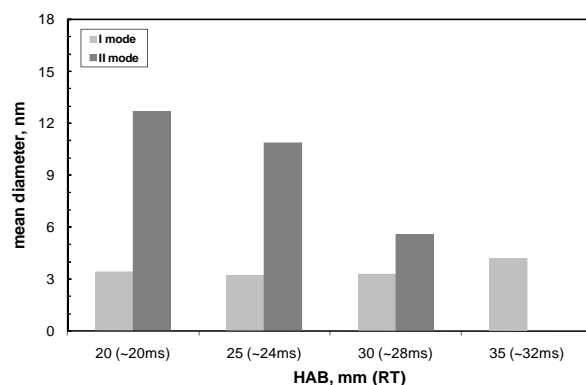
Figure 5. Mean diameters of the particles belonging to the first (I mode) and second mode (II mode) of the particle size distribution along the flame axis when injecting nickel(II) nitrate.

Similar to nickel(II) nitrate, lead(II) nitrate, which has even a lower solubility in water, fast nucleates in the droplets. The particle size distribution functions obtained by AFM analysis and their best fitting (parameters in Table III) are shown in Fig.6.

At HAB=20mm a broad size distribution function extending from 1 to 30nm is measured. The first mode particles (75% of particles number) have 6.3nm $<D>$ while a 15.6nm $<D>$ second mode is observed. A similar size distribution is observed at HAB=25mm whereas at HAB=30mm the two modes are more evident with the first mode having a quite smaller $<D>$ (4.4nm) and containing a slightly increased percentage (80%) of particle number. Slightly smaller MD (15.2nm) is measured also for the second mode. A further significant reduction of $<D>$ of each mode (2.9nm and 12.7nm) is observed at HAB=35mm whereas the relative number of particles into the first mode is almost the same.

Figure 6 also reports the AR versus particle diameter. Values ranging from 0.01 to 0.80, at HAB=20mm, and from 0.01 to 0.20, at HAB=25mm and 30mm, are observed showing that the larger particles have a solid nature. The AR lowering for heights larger than 25mm suggests melting of the nanoparticles along the flame axis.

The EDXS analysis reveals, as expected, the presence of lead, oxygen and nitrogen, the latter being more abundant at the first heights and decreasing at larger HAB.

Figure 7 summarizes the results reported in Fig.6a showing the change along the flame axis of the mean diameters of the first and second mode particles.

The time evolution of the size distribution shows a shrinking behavior similar to that observed for the $Ni(NO_3)_2$ case but generated particles have larger sizes and the bimodal size distribution function is observed at each sampling position. The larger sizes and polydispersion of the generated particles are related to the lower solubility in water of $Pb(NO_3)_2$ with respect to the other used metal salts. Indeed, solution saturation is reached faster and nuclei have much longer time to grow and aggregate into the droplets. Therefore, the smallest particles show larger diameter and larger particles represents a larger fraction of total respect to the other investigated cases. The particles shrinking at 30mm is justified by $Pb(NO_3)_2$ decomposition to PbO (690K-810K) [30] and its subsequent partial evaporation. PbO cannot further thermally decompose at 1200K. Then, thermal decomposition is unable to explain the further size reduction or the progressive relative number increase of smallest particles. For this reason, it is possible to assume that part of the PbO in vapor phase homogeneously nucleates generating 2.5nm particles at larger residence times where the temperature slightly decreases [21].
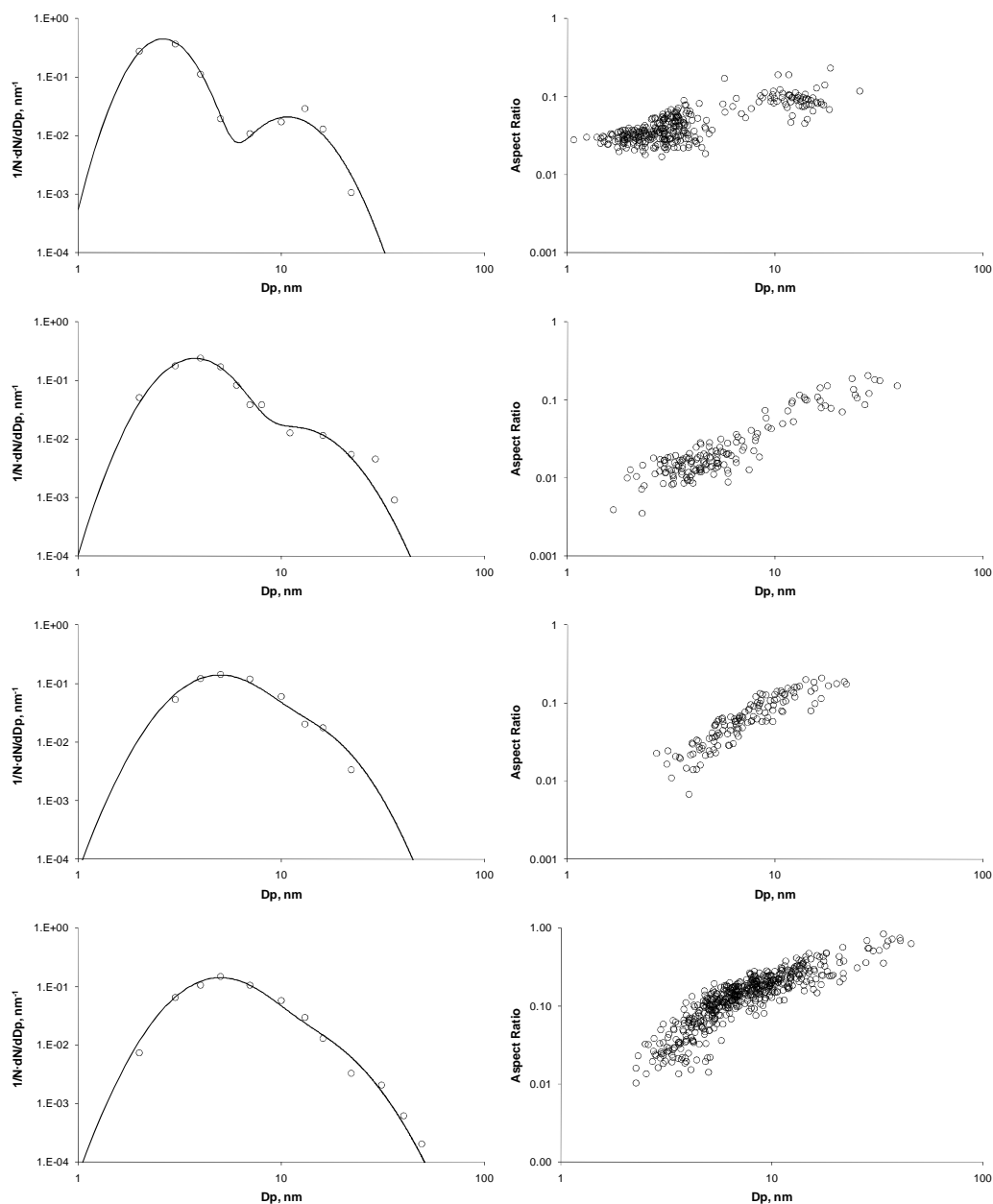
Figure 6. (left side) particle size distribution functions and (right side) aspect ratios measured along the flame axis when injecting lead(II) nitrate. From the bottom to the top: 20, 25, 30 and 35mm.
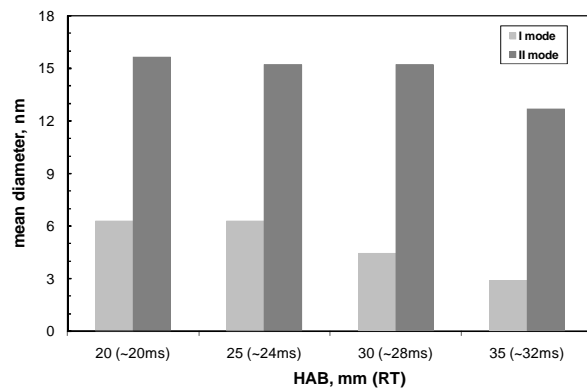

Figure 7. Mean diameters of the particles belonging to the first (I mode) and second mode (II mode) of the particle size distribution along the flame axis when injecting lead(II) nitrate.

We have compared the volume fractions of the thermophoretically collected matter with those determined by material balance. From the AFM size distribution functions, the total volume of the collected particles is determined. The ratio of the total volume of collected particles (Vol_{part}) and the sampled gas volume (Vol_{samp}) furnishes the volume fraction of the particles thermophoretically collected (see eq.1). Discrepancies between thermophoretic volume fractions and particle volume fractions determined by mass balance can be attributed to the capability of the particles of different sizes to remain attached on the substrate at relatively high temperature. We have here defined the capability to remain attached as an average particle adhesion efficiency (γ_{adh}) on the sampling mica disk:

$$\gamma_{adh} = \frac{V_{part}}{V_{imp}} = \frac{V_{par}}{fv \cdot V_{sam}} = \frac{fv_{AFM}}{fv}$$

(5)

The volume fraction of CdO nanoparticles thermophoretically collected is very low with respect to that determined by mass balance. At the beginning of the process, when only particles smaller than 5nm are collected, it is just 0.15% of the volume fraction of the particle present in the flame reactor. This percentage increases by about one order of magnitude simultaneously with the appearance of the second mode larger particles. A similar behavior is also shown by nickel- and lead-particles: the amount of the particles collected by thermophoresis decreases by orders of magnitude as particle size decreases at larger HAB.
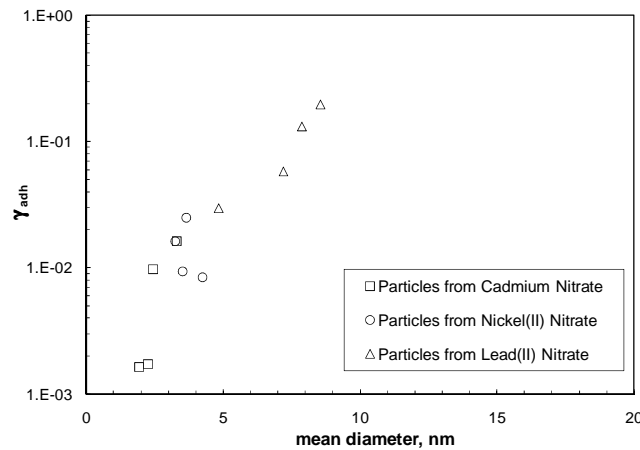

Figure 8. Adhesion efficiency as a function of the mean diameter of particles collected on the substrate.

Figure 8 reports the mean particle adhesion efficiency calculated by eq. 5 as a function of the mean diameter of collected particles. γ_{adh} is of the order of 10^{-3} for particle with mean sizes below 5nm and reaches values as high as 0.3 for particle with mean size of the order of 10nm. Metal vaporization and the assumption on particle densities made to calculate their volume fraction can affect the calculated absolute value of the adhesion efficiency. Nevertheless the uncertainty induced by both not considering the vaporization and hypothesizing particle density, cannot affect the efficiency variation by orders of magnitude for different particles size. Indeed the size distribution functions have quite different time evolutions whereas particle density cannot change by orders of magnitude.

A similar behavior of the adhesion efficiency has been already observed for carbonaceous particles in the same size range and it has been explained with the simplest assumption that all the particles with a thermal kinetic energy which is larger than the interaction energy will escape and rebound elastically if their residence time in the potential well is very short [31]. The adhesion efficiency at medium high temperature seems not macroscopically influenced by the chemical nature of the particles but it is strongly affected by the sizes. The low adhesion efficiency of very small particles is interesting in developing filtering systems able to capture a huge number of particles in the ultrafine range. It is worthwhile remarking that the interaction energy of very small nanoparticles at high temperature is of the order of their kinetic energy, which opens the way to much more advanced modelling based on quantum mechanism and molecular dynamics.

Conclusions

The size distributions, in a size range extending down to 1nm, of nanoparticles generated by quickly heating cadmium, nickel(II) and lead(II) nitrate aqueous solution droplets in a flame exhaust gases, have been measured with the AFM technique.

Despite the different behavior of the particles size distribution functions measured for the different metals, particles smaller than 10nm are formed and collected in each investigated case. Results suggest that nanoparticles nucleate inside the droplets during their fast not-uniform heating/vaporization/dehydration, and their sizes seem correlated with solubility in water and dehydration temperature of the salt precursor. Almost monodisperse ~2nm CdO particles were generated using the highest soluble and faster dehydrating $Cd(NO_3)_2$. The bimodal nature and slight larger diameters of nanoparticles produced from $Ni(NO_3)_2$, depends on its slightly lower solubility and dehydrating temperature over $Cd(NO_3)_2$, involving faster nitrate nucleation. Therefore, nuclei are able to slightly grow and some of them to coagulate before emerging from the droplets. The smallest nuclei were almost instantaneously heated and decomposed to NiO ~3nm particles while larger ones decomposition required longer time because of lower specific surface area slowing nitrides release. Larger first mode particles and higher frequency of second mode are obtained from the less soluble $Pb(NO_3)_2$ because of its faster nucleation into the droplets. This particles shrink because of $Pb(NO_3)_2$ to PbO decomposition. This decomposition is slower respect to that of $Ni(NO_3)_2$ because larger particles were produced.

Small nanoparticles show to rebound when colliding on the mica substrate, resulting in very low adhesion efficiency. The adhesion efficiency is not macroscopically influenced by the chemical nature of the particles but it is strongly affected by the sizes. The size dependence of the adhesion efficiency quantitatively agree for all the investigate cases and with that reported in literature for carbonaceous nanoparticles [31]. This feature is interesting in developing filtering systems able to remove nanoparticles with size lower than 5nm at the exhaust of combustion systems.

The inability to remove metal nanoparticles smaller than 10nm imply a not-trivial pollution problem because, due to their small volume, they are released at the exhaust of combustion devices and persist in atmosphere in high number concentration even if they represent a small mass percentage of particulate matter.

References

[1]   Lighty, J.A.S., Veranth, J.M., Sarofim, A.F., "Combustion aerosols: factors governing their size and composition and implications to human health", *J. Air & Waste Manage. Assoc.* 50: 1565-1618 (2000).

[2]   Brown, D.M., Wilson, M.L., MacNee, W., Stone, V., Donaldson, K., "Size-Dependent Proinflammatory Effects of Ultrafine Polystyrene Particles: A Role for

Surface Area and Oxidative Stress in the Enhanced Activity of Ultrafines", *Toxicol. Appl. Pharmacol.* 175: 191-199 (2001).

[3]   Oberdorster, G., Oberdorster, E., Oberdorster, "Concepts of Nanoparticle Dose Metric and Response Metric", *J., Environ. Health Perspectives* 113: 823-839 (2005).

[4]   Kennedy, I.M., "The health effects of combustion-generated aerosols", *Proc. Combust. Inst.* 31: 2757-2770 (2007).

[5]   Biswas, P., Wu, C.Y., "Nanoparticles and the environment", *J. Air & Waste Manage. Assoc.* 55:708–746 (2005).

[6]   Haynes, B.S., Wagner, H. G., "Soot formation", *Prog. Energy Combust. Sci.* 7: 229-273 (1981).

[7]   Bockhorn, H., D'Anna, A., Sarofim, A.F., Wang, H., *Combustion Generated Fine Carbonaceous Particles*, Karlsruhe University Press, 2009.

[8]   D'Anna, A., "Combustion-formed nanoparticles", *Proc. Combust. Inst.* 32: 593-613 (2009).

[9]   Linak, W.P., Wendt, J.O.L., "Toxic metal emissions from incineration: Mechanisms and control", *Prog. Energy Combust. Sci.* 19: 145-185 (1993).

[10]   Carbone, F., Beretta, F., D'Anna, A., "A Flat Premixed Flame Reactor to study Nano-Ash Formation during High Temperature Pulverized Coal Combustion and Oxygen Firing"*, Fuel* 90: 369-375 (2010).

[11]   Carbone, F. , Beretta, F., D'Anna, A., "Multimodal ultrafine particles from pulverized coal combustion in a laboratory scale reactor", *Combust. Flame* 157: 1290-1297 (2010).

[12]   Carbone, F. , Beretta, F., D'Anna, A., "Factors Influencing Ultrafine Particulate Matter ($PM_{0.1}$) Formation under Pulverized Coal Combustion and Oxyfiring Conditions", *Energy and Fuels* 24: 6248-6256 (2010).

[13]   Helble, J.J., Sarofim, A.F., "Factors determining the primary particle size of flame-generated inorganic aerosols", *J. Colloid Interface Sci.* 128: 348-362 (1989).

[14]   Matsoukas, T., Friedlander, S.K., "Dynamics of aerosol agglomerate formation", *J. Colloid Interface Sci.* 146: 495-506 (1991).

[15]   Mulholland, J.A., Sarofim, A.F., "Mechanisms of inorganic particle formation during suspension heating of simulated aqueous wastes", *Environ. Sci. Technol.* 25: 268-274 (1991).

[16]   Merola, S.S., Kurz, M., Borghese, A., D'Anna, A., D'Alessio, A., "Ultraviolet Broadband Light Scattering by Single Metal-containing Droplets Combustion Science and Technology", *Combust. Sci. Tech.* 134: 221-241 (1998).

[17]   Ehrman, S., Friedlander, S.K., "Bimodal distributions of two component metal oxide aerosols", *Aerosol Science and Technology* 30: 259–272 (1999).

[18]   Biswas, P., Zachariah, M.R., "In Situ Immobilization of Lead Species in Combustion Environments by Injection of Gas Phase Silica Sorbent Precursors", *Environ. Sci. Technol.* 31: 2455-2463 (1997).

[19]   Fennell, P.S., Dennis, J.S., Hayhurst, A.N., "The sampling of nanoparticles of MgO formed when doping an oxygen-rich flame with magnesium: The measurement of the concentrations and size-distributions of these nanoparticles", *Combust. Flame* 151: 560-572 (2007).

[20]   Barone, A.C., D'Alessio, A., D'Anna, A., "Morphological characterization of the early process of soot formation by atomic force microscopy", *Combust. Flame* 132: 181-187 (2003).

[21]   Carbone, F., Barone, A.C., Pagliara, R., Beretta, F., D'Anna, A., D'Alessio, A., "Ultrafine particles formed by heating droplets of simulated ash containing metals", *Environ. Eng. Sci.* 25: 1379-1387 (2008).

[22]   Carbone, F., *Physicochemical Characterization of Combustion Generated Inorganic Nanoparticles. PhD dissertation in Chemical Engineering 2008, Università degli Studi di Napoli Federico II*, Fredericiana Editrice Universitaria, 2010.

[23]   Friedlander, S. K. *Smoke, Dust and Haze*, Oxford University Press, 2000.

[24]   Hinds, W. C., *Aerosol Technology: Properties,Behavior and Measurement of Airborne Particles*, John Wiley & Son, 1999.

[25]   Limaye, A.U., Helble, J.J., "Morphological control of zirconia nanoparticles through combustion aerosol synthesis", *J. Am. Ceram. Soc.* 85: 1127-1132 (2002).

[26]   Lanotte, L., Ausanio, G., Barone, A.C., Hison, C., Iannotti, V., Amoruso, S., Bruzzese, R., Vitiello, M., D'Incau, M., Scardi, P., "Peculiarities and potentialities of ultra-short pulsed laser deposition for the production of magnetic nanogranular films", *J. Opt. Adv. Mater.* 8: 1672-1678 (2006).

[27]   Zhao, B., Uchikawa, K., Wang, H., "A comparative study of nanoparticles in premixed flames by scanning mobility particle sizer, small angle neutron scattering, and transmission electron microscopy", *Proc. Combust. Inst.* 31: 851-860 (2007).

[28]   Wojciechowski, K. T., Malecki, A., "Mechanism of thermal decomposition of cadmium nitrate $Cd(NO_3)_2 \cdot 4H_2O$", *Thermochimica Acta* 331: 73-77 (1999).

[29]   Brockner, W., Ehrhardt, C., Gjikaj, M., "Thermal decomposition of nickel nitrate hexahydrate, $Ni(NO_3)_2 \cdot 6H_2O$, in comparison to $Co(NO_3)_2 \cdot 6H_2O$ and $Ca(NO_3)_2 \cdot 4H_2O$", *Thermochimica Acta* 456: 64-68 (2007).

[30]   Stern, K. H., "High Temperature Properties and Decomposition of Inorganic Salts Part 3, Nitrates and Nitrites", *J. Phys. Chem. Ref. Data* 1: 747-772 (1971).

[31]   D'Alessio, A., Barone, A.C., Cau, R., D'Anna, A., Minutolo, P., "Surface deposition and coagulation efficiency of combustion generated nanoparticles in the size range from 1 to 10 nm", *Proc. Combust. Inst.* 30: 2595-2603 (2005).